Supporting Information

Phosphorus-doped Porous Hollow Carbon Nanorods for High-performance Sodium Based Dual-ion Battery

Xiaoyan Wang, Shaofeng Wang, Kaixiang Shen, Shenggong He, Xianhua Hou* Fuming Chen*

Guangdong Provincial Key Laboratory of Quantum Engineering and Quantum Materials, Guangdong Engineering Technology Research Center of Efficient Green Energy and Environment Protection Materials, Engineering Research Center of MTEES (Ministry of Education), School of Physics and Telecommunication Engineering, South China Normal University, Guangzhou 510006, China

* Corresponding author: *fmchen@m.scnu.edu.cn (F.C.); houxianhua@m.scnu.edu.cn (X. H.)*

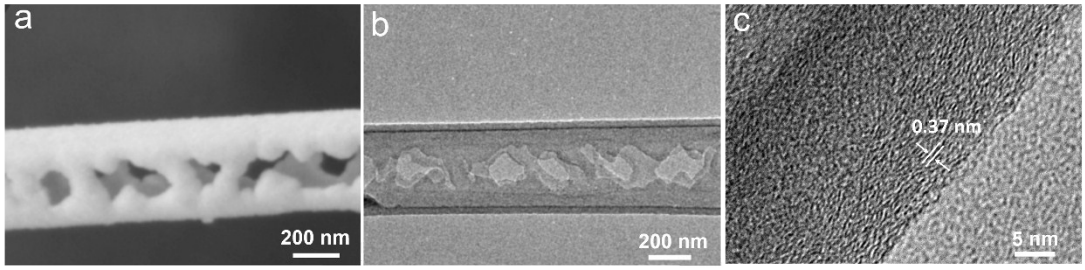

Figure S1. (a, b) SEM and TEM of signal HCNs. (c) HRTEM of P-HCNs.

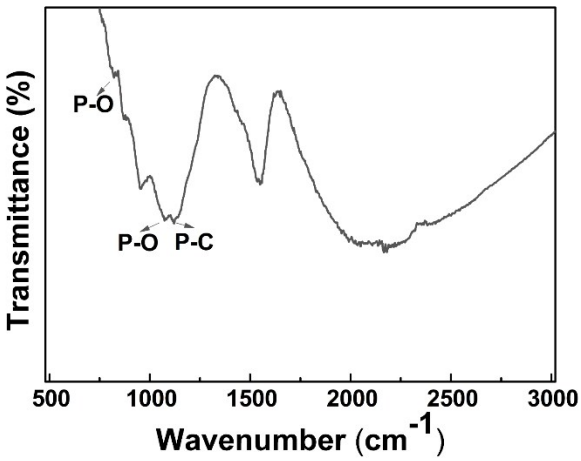

Figure S2. FTIR curve of P-HCNs, 1120.50 cm^{-1} is assigned to P-C swing and C=C stretching, and the peak located at 1063.8 cm^{-1} is accounted for coupling of P-O symmetric stretching and P-C.

29

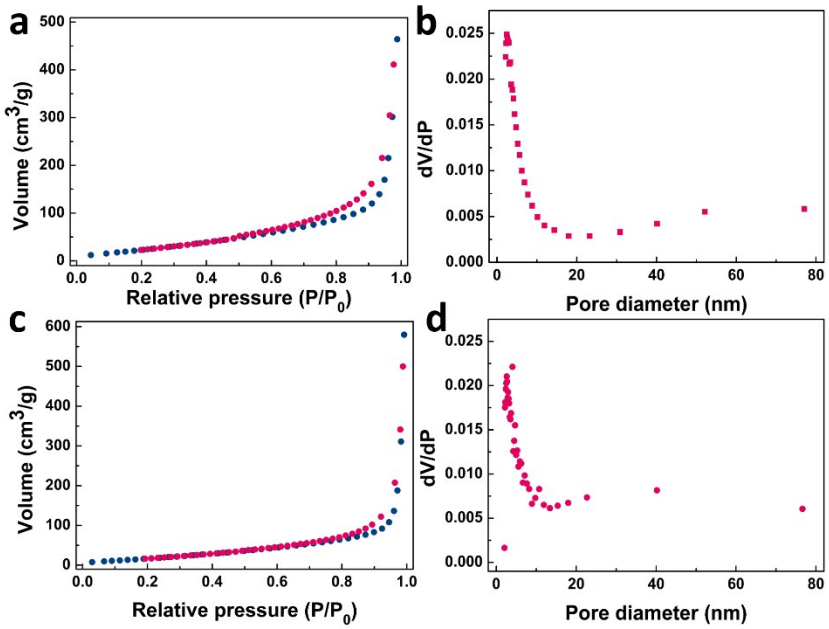

30

31 **Figure S3**. Nitrogen adsorption/desorption isotherms and the pore diameter of (a, b) HCNs and (c,

32 d) P-HCNs.

33

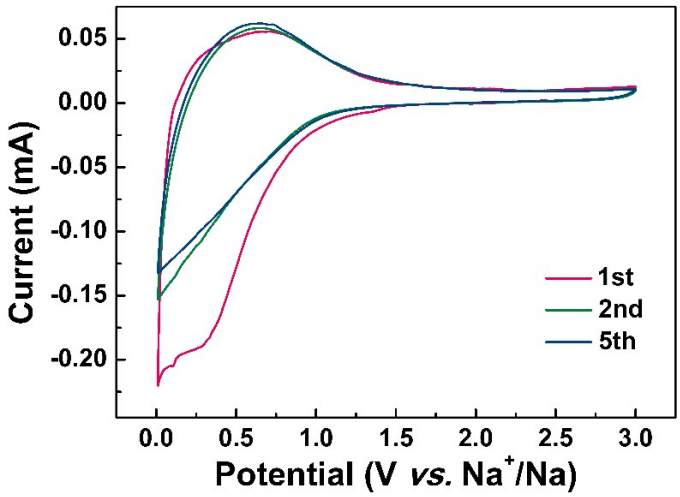

Figure S4. CV cures of HCNs in the potential range of 0.01-3.0 V at the scan rate of 0.2 mVs^{-1}

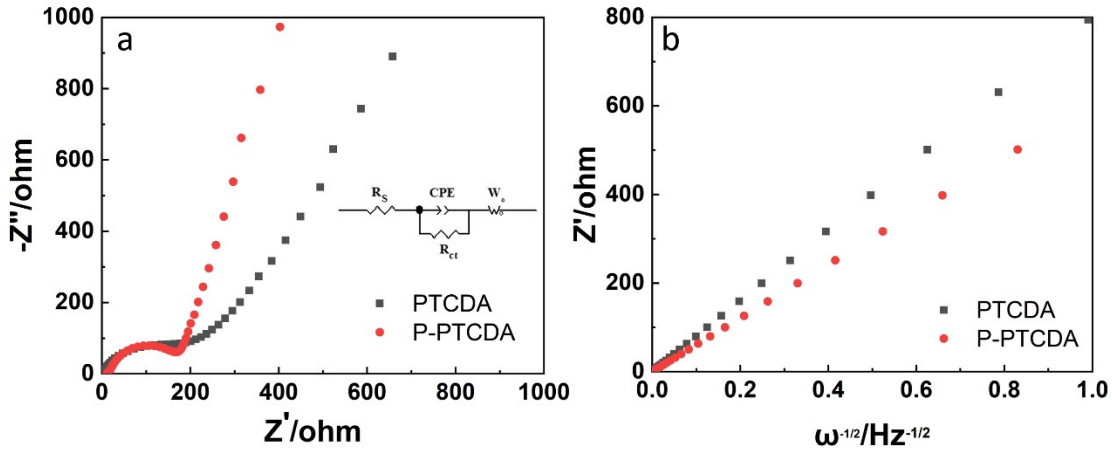

Figure S5 (a) Nyquist plots of the NIBs based on P-HCNs anode. (b) Warburg impedance, Z' as a function of $\omega^{-1/2}$.

Diffusion coefficient value for Na-ion in case of HCN and P-HCN was calculated by the following equation:[1]

$$D = \frac{R^2T^2}{2\sigma^2n^4F^4A^2C^2}$$

R is the gas constant，T is the Kelvin of thermodynamic temperature (293K), σ is the Warburg coefficient, n is electron transfer number (n=1), F is the Faraday's number (96485.33289±0.00059C/mol), A is electrode area and C is the concentration of sodium in the electrode. The 2032 type of half-cell was assembled for EIS test. The electrode area is π (0.6 cm)^2. When the battery is full discharged, sodium and carbon can form NaC6 compounds, which likes Li inserting to carbon. The mass of active material is 0.8 mg, so C= $\frac{0.8\times10^{-3}}{12}\times\frac{1}{6}\times\frac{1}{\pi\,0.6^2}$. Because the thickness of the electrode is less than 20 um, so the volume of the electrode is approximately calculated equal to π (0.6 cm)^2. Finally, the diffusion coefficient value for Na-ion in case of HCN and P-HCN are about 6.7×10^{-16} and 11.8×10^{-16} cm^2/S, respectively

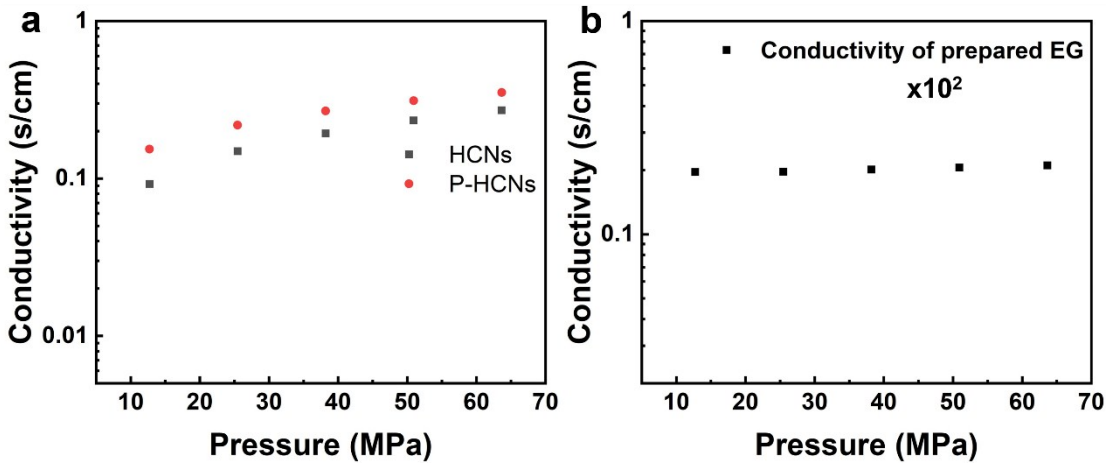

Figure S6 (a) Pressure-Conductivity graph of HCNs and P-HCNs. (b) Pressure-Conductivity graph of EG.

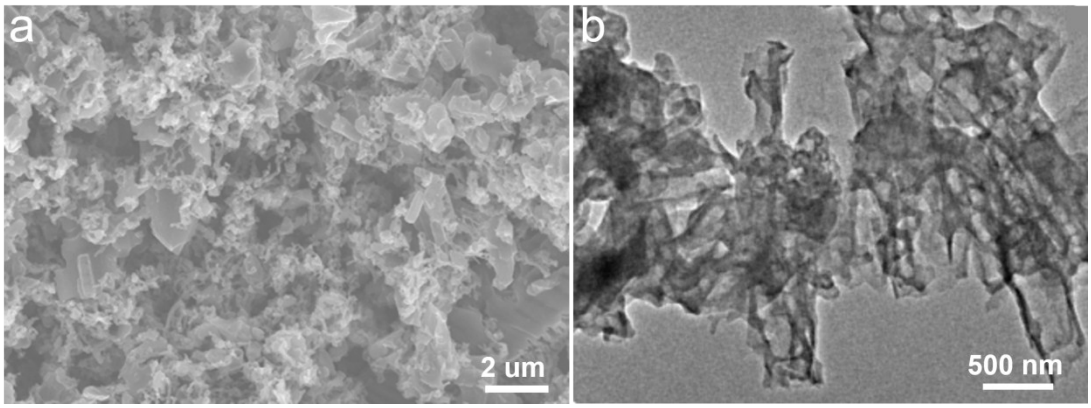

Figure S7. (a) SEM, (b) TEM image of P-HCNs for half-cell after 500 cycles at the current density of 500 mA g^{-1}.

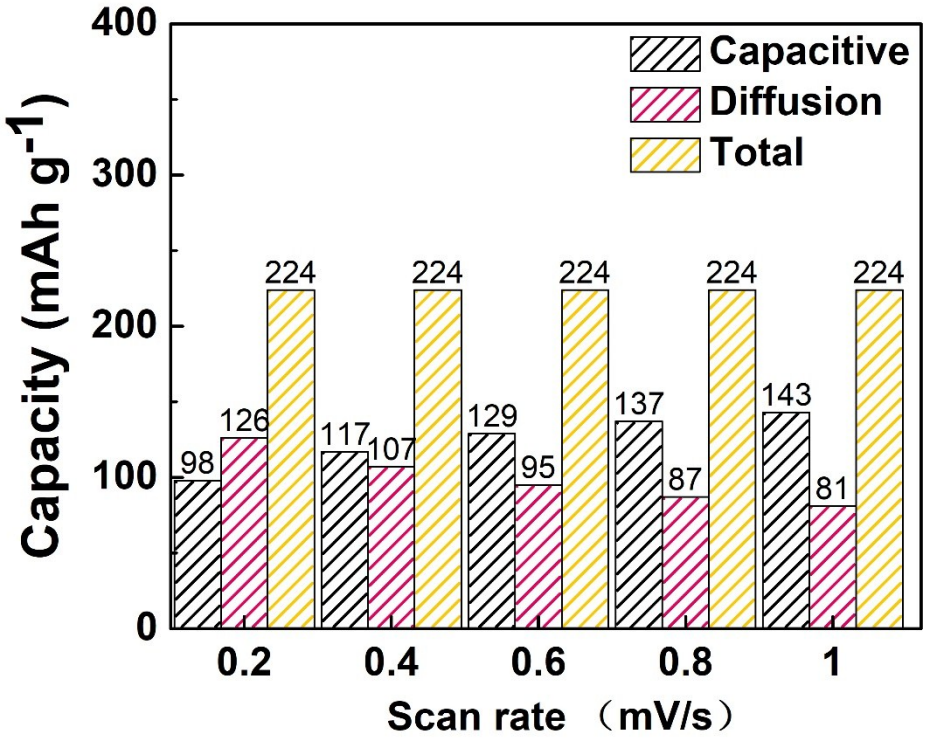

Figure S8 Capacitive, diffusion-control and total capacities for varied scan rates of P-HCNs electrode.

Note S1

To better testify that PF_6^- has involved in the insertion and desertion processes for NDIBs, the Ex-situ XRD patterns of EG cathode at different charge/discharge states (Figure S9a) are carried out in Figure S9b. There is only one characteristic graphite (002) peak at $2\theta = 23.8^\circ$. Once charged from 3.5-4.7 V, the (002) peak shifts to a lower angle, indicating a gradually increased layer spacing during the PF_6^- interposed into the EG cathode. While discharged from 4.7 V to 2.0 V, the (002) peak recovers approached to 23.8° , which means the PF_6^- de-intercalation from EG. Different from the initial stage, the (002) peak of EG becomes broad and decline, meaning reduced crystallinity. It is because of the formation of SEI in charge process. Ex-situ XPS spectra in Figure S9c are performed to further study the PF_6^- reacted with EG. In the pristine state, it only exhibits two peaks around 285.0 eV and 534.0 eV, assigning to C 1s, and O 1s. When charged to 4.7 V, three new peaks appear around 192.7 eV and 823.0 eV, meaning P 2p, F 1s and Na 1s, respectively. The increased Na and F contents in fully charged state at 4.7 V suggests that PF_6^- has inserted into the EG cathode. When discharged to 2 V, the intensity of F 1s and Na 1 is reduced obviously, demonstrating that PF_6^- release from EG to the electrolyte. Figure S9d is the high-resolution F1s XPS of P-HCNs, it reflects that the F element for EG is attributed to the formation of NaF in the EG electrode of NDIBs after the initial cycles.

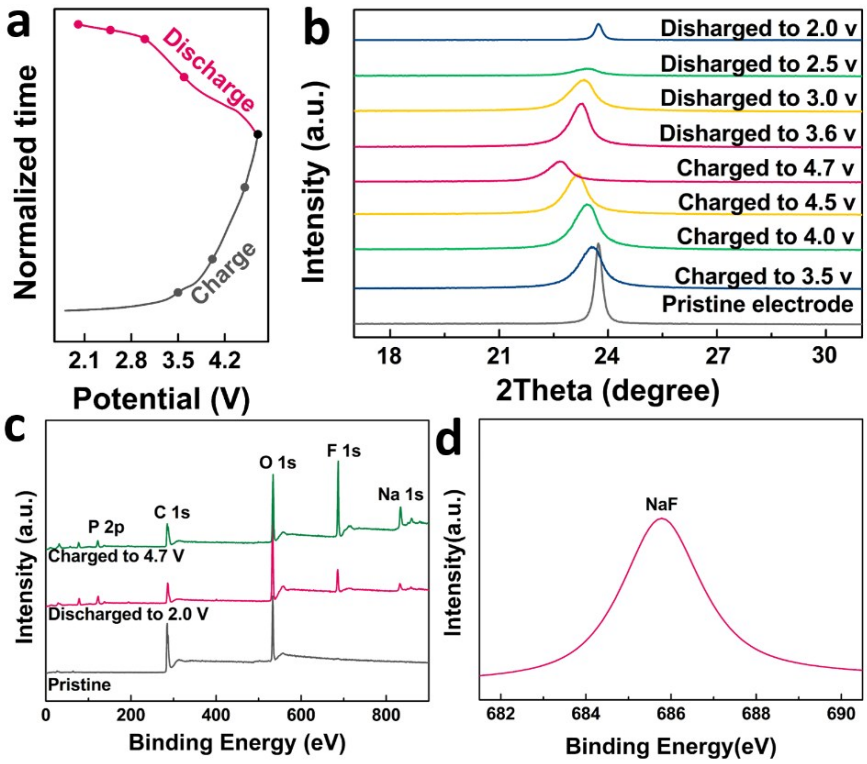

Figure S9 (a) Normalized voltage-time curves of full cell. (b) The ex-situ XRD patterns of the EG at different states during initial charge/discharge process. (c) The full XPS spectra of the EG electrodes at different state after one cycle. (d) The high-resolution F1s XPS of the EG.

Note S2

The morphology of EG was investigated by SEM and TEM in Figure S10a-10c. The layer spacing is 0.373 nm as shown in Figure S10c, which is larger than graphite (0.3354 nm). The XRD pattern of EG (Figure S10d) shows only one peak at 23.8°, assigned to the (002) plane. Figure S10e displays the charge/discharge curves of EG cathode within the potential window of 2.0-4.7 V. The first CE is 55.0%. After 100 cycles, the reversible capacity of 105 mAh g^{-1} can be still obtained for the EG electrode as demonstrated in Figure S10f.

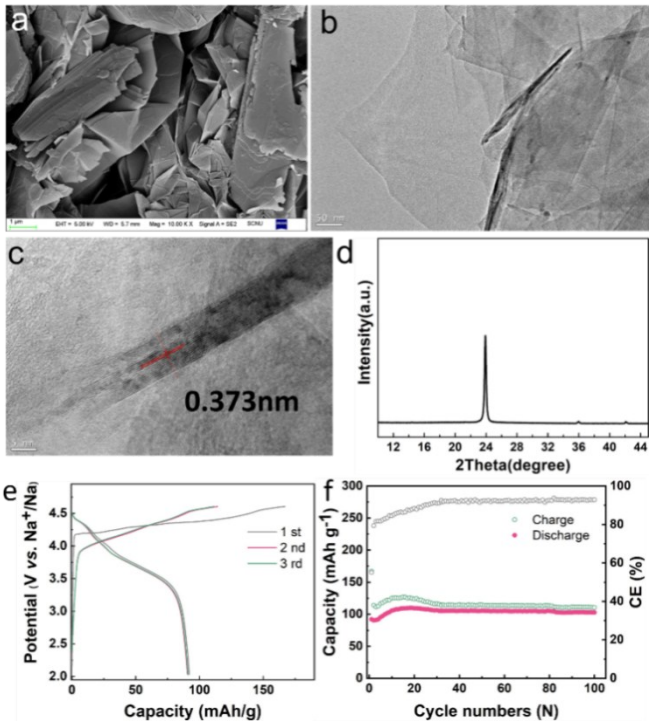

Figure S10 (a) SEM image of as-prepared EG, (b) TEM image of as-prepared EG, (c) HR-TEM image of as-prepared EG, (d) XRD patterns of prepared EG. (e) The charge/discharge curves of EG cathode in half-cell within the potential windows of 2.0-4.7 V, (f) The cycling performance of EG at 100 mA g^{-1}.

Table S1 The atomic content of C, O and P in P-HCNs analyzed by EDS.

Materials P-HCN	Element Content by atomic (%)
C	88.4
O	10.2
P	1.4

Note S3: Energy density and power density calculation of P-HCNs//EG NDIBs.

The power and energy densities were calculated by the following formula[2]:

$$E = \int_{t1}^{t2} IVdt = \frac{1}{2}C(V_{max} + V_{min})(V_{max} - V_{min}) = \frac{V_{max} + V_{min}}{2} \times \frac{It}{m} \times \frac{1}{3.6} \quad (1)$$

$$p = \frac{3600 \times E}{t} \quad (2)$$

where V_{max} and V_{min} are the initial and final discharge voltages (V), I is the discharge current (A), t is the discharge time (s), m is the total mass of the anode and cathode active material (mg), E is the energy density (Wh kg^{-1}), and P is the power density (W kg^{-1}). For example, when the discharge current density is maintained at 0.2 A g^{-1} for 57.75×60 s, and the total mass of anode and cathode active materials is 3.12 mg, the energy and power densities can be calculated as below:

$$E = \frac{2.00509 + 4.698}{2} \times \frac{0.2 \times 0.8 \times 57.75 \times 60}{3.12} \times \frac{1}{3.6} = 165 \text{ Wh kg}^{-1} \quad (3)$$

$$p = \frac{3600 \times E}{t} = \frac{3600 \times 165}{57.75 \times 60} = 171\ \mathrm{W\ kg^{-1}} \quad (4)$$

Calculated from the same method as above, the energy and power densities at different current density could be obtained, which are showed in Table S2**.**

Table S2. A summary of the performance of reported devices

Anode//Cathode	Potential range (V)	E (Wh/kg)	P (W/kg)	Current density (A g^{-1})
CNT//V_2O_5[3]	1.8-4.0	40	210	-
TiO_2-Graphene//AC[4]	1-3.8	64.2	56.3	3.35
Graphene//GMP[5]	0-1.8	42.3	950	10
Nb_2O_5@C/rGO//AC[6]	1–4.3	76	80	1
C//AC[7]	0–4.0	112	67	5
TNW//CNT[8]	0-2.8	12.5	300-320	10C
400-KON-Ti3C2[9]	0-1.6	27.4	--	1
	0-1.6	17.1	4	--
HAT-CNF//Carbon[10]	0.5-4.0	95	190	--
	0.5-4	65	1800	--
$Na_3V_2(PO_4)_3$@C//AC[11]	0-3.0	118	95	--
	0-3.0	60	850	--
This work	**2-4.7**	**76**	**891**	**1**
	2-4.7	**69**	**1821**	**2**
	2-4.7	**103**	**906**	**0.8**
	2-4.7	**143**	**580**	**0.5**
	2-4.7	**165**	**171**	**0.2**

Reference

[1] H. Liu, Q. Cao, L.J. Fu, C. Li, Y.P. Wu, H.Q. Wu, Doping effects of zinc on $LiFePO_4$ cathode material for lithium ion batteries, Electrochemistry Communications, 8(10）1553-1557.

[2] X. Ren, Z. Ren, Q. Li, W. Wen, X. Li, Y. Chen, L. Xie, L. Zhang, D. Zhu, B. Gao, Tailored Plum Pudding-Like Co2P/Sn Encapsulated with Carbon Nanobox Shell as Superior Anode Materials for High-Performance Sodium-Ion Capacitors, Advanced Energy Materials, (2019).

[3] Z. Chen, V. Augustyn, J. Wen, Y. Zhang, M. Shen, B. Dunn, Y. Lu, High-performance supercapacitors based on intertwined CNT/V2O5 nanowire nanocomposites, Advanced Materials, 23 (2011) 791-795.

[4] Z. Le, F. Liu, P. Nie, X. Li, X. Liu, Z. Bian, G. Chen, H.B. Wu, Y. Lu, Pseudocapacitive sodium storage in mesoporous single-crystal-like TiO2–graphene nanocomposite enables high-performance sodium-ion capacitors, ACS nano, 11 (2017) 2952-2960.

[5] J. Fu, J. Yun, S. Wu, L. Li, L. Yu, K.H. Kim, Architecturally Robust Graphene-Encapsulated MXene Ti2CT x@ Polyaniline Composite for High-Performance Pouch-Type Asymmetric Supercapacitor, ACS applied materials & interfaces, 10 (2018) 34212-34221.

[6] E. Lim, C. Jo, M.S. Kim, M.H. Kim, J. Chun, H. Kim, J. Park, K.C. Roh, K. Kang, S. Yoon, Hybrid Supercapacitors: High-Performance Sodium-Ion Hybrid Supercapacitor Based on Nb2O5@Carbon Core–Shell Nanoparticles and Reduced Graphene Oxide Nanocomposites (Adv. Funct. Mater. 21/2016), Advanced Functional Materials, 26 (2016) 3553-3553.

[7] H. Wang, D. Mitlin, J. Ding, Z. Li, K. Cui, Excellent energy–power characteristics from a hybrid sodium ion capacitor based on identical carbon nanosheets in both electrodes, Journal of Materials Chemistry A, 4 (2016) 5149-5158.

[8] Q. Wang, Z. Wen, J. Li, A hybrid supercapacitor fabricated with a carbon nanotube cathode and a TiO2–B nanowire anode, Advanced Functional Materials, 16 (2006) 2141-2146.

[9] J. Li, X. Yuan, C. Lin, Y. Yang, L. Xu, X. Du, J. Xie, J. Lin, J. Sun, Achieving high pseudocapacitance of 2D titanium carbide (MXene) by cation intercalation and surface modification, Advanced Energy Materials, 7 (2017) 1602725.

[10] R. Yan, E. Josef, H. Huang, K. Leus, M. Niederberger, J.P. Hofmann, R. Walczak, M. Antonietti, M. Oschatz, Understanding the Charge Storage Mechanism to Achieve High Capacity and Fast Ion Storage in Sodium-Ion Capacitor Anodes by Using Electrospun Nitrogen-Doped Carbon Fibers, Advanced Functional Materials, (2019) 1902858.

[11] K. Kaliyappan, Going Beyond Lithium Hybrid Capacitors: Proposing a New High-Performing Sodium Hybrid Capacitor System for Next-Generation Hybrid Vehicles Made with Bio-Inspired Activated Carbon, Advanced Energy Materials, 6 (2016).